# Numerical Simulation of Water-Gas Flow in Low Permeability Reservoirs

Gillyan Macário da Silva

Pós-graduação em Modelagem Computacional, Instituto Politécnico, Universidade do Estado do Rio de Janeiro, Brasil.

Mayksoel Medeiros de Freitas

Departamento de Engenharia Mecânica e Energia, Instituto Politécnico, Universidade do Estado do Rio de Janeiro, Brasil.

Grazione de Souza

Departamento de Modelagem Computacional, Instituto Politécnico, Universidade do Estado do Rio de Janeiro, Brasil.

Helio Pedro Amaral Souto

Departamento de Modelagem Computacional, Instituto Politécnico, Universidade do Estado do Rio de Janeiro, Brasil.

Abstract: Natural gas recovery has increased with the production from unconventional reservoirs with low absolute permeability. In these reservoirs, production is favored, for example, by the use of horizontal wells and the gas-phase slippage effect. This work performs a numerical simulation of two-phase isothermal water-gas flow, accounting for the impact of gas slip and permeability variation as a function of the stress change acting on the porous matrix. The governing equations are discretized using the Finite Volume Method. The obtained algebraic equation systems are linearized and solved by applying a Picard-Newton solution strategy, an operator splitting method, and the iterative preconditioned Stabilized Biconjugate Gradient method. The results are presented in terms of instantaneous gas flow rate and recovered gas volume, considering several production scenarios for the prescribed well pressure. In conclusion, the results showed that it was possible to capture the incorporated physical effects, with slippage favoring production and the change due to the stress effect leading to a decrease in apparent permeability resulting from the pressure drop caused by production.

Palavras-chave: horizontal well, low permeability reservoirs, Picard-Newton method, two-phase flow.

Corresponding author: Helio Pedro Amaral Souto, helio@iprj.uerj.br

Received: 08 Jul 2025 / Accepted: 20 Jul 2025 / Published: 11 Aug 2025.

## 1 Introduction

The increasing global energy demand has driven the exploration and production of unconventional oil and gas sources [4]. Among the significant available resources are gas reservoirs characterized by low permeability, often referred to as tight gas reservoirs. Production from these reservoirs presents unique challenges due to their inherent low permeability and porosity, as well as their structural complexity [1, 17]. To overcome these difficulties and make production viable, advanced techniques like hydraulic fracturing and horizontal drilling are widely employed [8]. Furthermore, multiphase flow introduces additional complications [21], such as production limitations caused by the presence of water, which can occupy pore spaces and impede gas flow [5].

According to Xu et al. [23], the presence of water in pores and fractures significantly interferes with gas mobility in a two-phase flow context. Typically, numerical methods are utilized to study flow dynamics and predict production. The most sophisticated models integrate elements such as gas adsorption on the rock surface and incorporate mechanisms that account for gas slippage. Moreover, the injection of fluids during fracturing can alter reservoir properties, potentially creating low-permeability zones near the wellbore [15].

Several mechanisms in physical-mathematical modeling can explain the low water recovery often observed during production in these reservoirs. These include wa-

 

ter retention within the fracture network and water imbibition associated with osmotic and capillary pressure. As highlighted by He et al. [15], these factors hinder water flow, a phenomenon that can be effectively modeled using a modified version of Darcy's law for low-velocity flows. Consequently, the authors adapted Darcy's law to describe water transport and employed another version adjusted for gas transport, specifically considering slippage mechanisms and free molecular flow. The Klinkenberg effect, also known as gas slippage, occurs in low-permeability media where gas molecules achieve higher velocities near pore walls. This phenomenon is particularly relevant under low-pressure conditions and results in an effective (apparent) permeability that is greater than the absolute permeability [18].

On the other hand, effective stress can significantly impact the permeability of porous media. Compression of the porous medium, caused by increased pressure, can restrict fluid flow. This necessitates incorporating a relationship that describes permeability as a function of stress and deformation [22]. These effects become especially important in horizontal wells with hydraulic fracturing, where stress redistribution can alter flow behavior within open fractures. In contrast, conventional reservoirs typically trap hydrocarbons in porous and permeable rocks, generally allowing for natural migration and facilitated extraction.

Indeed, horizontal drilling represents an essential technology in the exploitation of unconventional reservoirs. It has radically transformed the oil and gas industry by enabling production from geological formations with inherently low permeability [2]. This technique involves diverting the well trajectory from a vertical to a horizontal or near-horizontal orientation relative to the main reservoir bedding, thereby maximizing the contact area between the well and the producing formation. Initially, the well is drilled vertically until it reaches a depth close to the target layer. Subsequently, a directional deviation is performed using specialized tools to change the well's trajectory. From this point, drilling continues horizontally along the producing layer for hundreds or even thousands of meters, significantly expanding the hydrocarbon drainage area.

In this work, we study two-phase water-gas flow during production in a low-permeability reservoir utilizing a horizontal well and numerical reservoir simulation techniques. Our primary contribution lies in addressing this challenging problem by proposing a novel solution approach: we employ the Picard-Newton method to accurately model situations where both slippage and stress effects significantly influence the apparent permeability.

## 2 Physical-mathematical modeling

Considering the Cartesian coordinate system, the mass balance for flow in porous media yields [7],

$$\frac{\partial}{\partial t}\left(\phi\rho_l S_l\right) + \nabla\cdot\left(\rho_l \mathbf{v}_l\right) - \dot{q}_{ml} = 0, \tag{1}$$

where $\phi$ is the porosity, and $\rho_l$, $S_l$, $\mathbf{v}_l$, and $\dot{q}_{ml}$ are, respectively, the specific mass, saturation, apparent velocity, and source term (mass per unit time per unit volume) for phase $l$.

For multiphase flows, the classical Darcy's law requires modification to account for the flow resistance that a given phase exerts on the others [11]. Furthermore, Darcy's law can be modified to incorporate effects such as slippage and the influence of effective stress.

Slippage, also known as the Klinkenberg effect, occurs when the pore size is comparable to the mean free path of gas molecules, with the effect being more noticeable at reduced pressures. The permeability value in these cases must be corrected, with the first model employed to capture this phenomenon being [18]

$$\mathbf{k}_{ag} = \left(1 + \frac{b}{p}\right)\mathbf{k}, \tag{2}$$

where $\mathbf{k}_{ag}$ is the apparent gas permeability, $\mathbf{k}$ the intrinsic permeability of the porous medium, $p$ the gas pressure, and $b$ the Klinkenberg factor.

On the other hand, in certain situations, permeability can be sensitive to variations in stress, which influences fluid flow within these formations. This phenomenon is known as the effective stress effect on permeability and can significantly impact gas production [14]. A simplified model used in the modeling of this effect is given by [25]

$$\mathbf{k} = e^{-\gamma(p_0 - p)}\mathbf{k}_0, \tag{3}$$

where $\gamma$ is the permeability modulus, dependent on the mineral composition and mechanical characteristics of the rock [24], $p_0$ is the initial pressure, and $\mathbf{k}_0$ represents the initial permeability (tensor considered diagonal here).

The concept of apparent permeability will be adopted for both phases. For the gas phase, $\mathbf{k}_{ag}$ takes into account the effects of slippage and effective stress, while for the water phase, $\mathbf{k}_{aw}$ considers only the effective stress effect. Thus, the modified Darcy's law is considered here in the form

$$\mathbf{v}_l = -\frac{k_{rl}}{\mu_l}\mathbf{k}_{al}\left(\nabla p_l - \lambda_l \nabla z\right) \tag{4}$$

where $\mathbf{k}_{al}$ is the apparent permeability tensor, $p_l$, $\mu_l$, and $k_{rl}$ are, respectively, the pressure, viscosity, and relative permeability of phase $l$, $\lambda_l = \rho_l g$, and $\nabla z$ is the depth gradient, with $g$ being the magnitude of gravitational acceleration.

Substituting Equation (4) into Equation (1),

$$\nabla\cdot\left[\frac{\rho_l k_{rl}}{\mu_l}\mathbf{k}_{al}\left(\nabla p_l - \lambda_l\nabla z\right)\right] = \frac{\partial}{\partial t}\left(\phi\rho_l S_l\right) - \dot{q}_{ml} \tag{5}$$

for each phase $l$, where $w$ represents the wetting phase (water), and $n$ designates the non-wetting phase (gas).

Expressing the specific mass of the phase in terms of the Formation Volume Factor (FVF), Equation (5) can be rewritten as [13]

$$\nabla\cdot\left[\frac{k_{rl}}{\mu_l B_l}\mathbf{k}_{al}\left(\nabla p_l - \lambda_l\nabla z\right)\right] = \frac{\partial}{\partial t}\left(\frac{\phi S_l}{B_l}\right) - \dot{q}_{scl} \tag{6}$$

where $B_l$ is the FVF of phase $l$ and $\dot{q}_{scl} = \dot{q}_{ml}/\rho_{scl}$, with $\dot{q}_{scl}$ being a volumetric flow rate source term under standard conditions and $\rho_{scl}$ the specific mass under standard conditions of phase $l$.

Assuming that the medium is fully saturated, we have [11],

$$S_{\mathtt{w}} + S_{\mathtt{g}} = 1, \tag{7}$$

where $S_{\mathtt{w}}$ is the saturation of the wetting phase and $S_{\mathtt{g}}$ is the saturation of the non-wetting phase.

Now, from the equation that provides the capillary pressure as a function of the phase pressures [7],

$$p_c = p_{\mathtt{g}} - p_{\mathtt{w}}, \tag{8}$$

the water pressure can be written in terms of the gas pressure and the capillary pressure.

From Equation (6), $S_{\mathtt{g}} = 1 - S_{\mathtt{w}}$, and $p_{\mathtt{w}} = p_{\mathtt{g}} - p_c$, we obtain for the gas phase

$$\nabla \cdot \left[ \frac{k_{r\mathtt{g}}}{\mu_{\mathtt{g}} B_{\mathtt{g}}} \mathbf{k}_{ag} \left( \nabla p_{\mathtt{g}} - \lambda_{\mathtt{g}} \nabla z \right) \right] = \frac{\partial}{\partial t} \left[ \frac{\phi (1 - S_{\mathtt{w}})}{B_{\mathtt{g}}} \right] - \dot{q}_{sc\mathtt{g}} \tag{9}$$

and, for the water phase,

$$\nabla \cdot \left[ \frac{k_{r\mathtt{w}}}{\mu_{\mathtt{w}} B_{\mathtt{w}}} \mathbf{k}_{aw} \left( \nabla p_{\mathtt{g}} - \nabla p_c - \lambda_{\mathtt{w}} \nabla z \right) \right] = \frac{\partial}{\partial t} \left( \frac{\phi S_{\mathtt{w}}}{B_{\mathtt{w}}} \right) - \dot{q}_{sc\mathtt{w}}, \tag{10}$$

where it was considered that $w = \mathtt{w}$ (water) and $n = \mathtt{g}$ (gas).

In this work, the modified Corey model is employed for the wetting phase [11], such that

$$k_{r\mathtt{w}}(S_{\mathtt{w}}) = k_{r\mathtt{w}_{max}} \left( \frac{S_{\mathtt{w}} - S_{i\mathtt{w}}}{1 - S_{i\mathtt{w}} - S_{gr\mathtt{w}}} \right)^{e\mathtt{w}} \tag{11}$$

and, for the non-wetting phase,

$$k_{r\mathtt{g}}(S_{\mathtt{w}}) = k_{r\mathtt{g}_{max}} \left( \frac{1 - S_{\mathtt{w}} - S_{gr\mathtt{w}}}{1 - S_{i\mathtt{w}} - S_{gr\mathtt{w}}} \right)^{eo\mathtt{w}}, \tag{12}$$

where $S_{\mathtt{w}}$ and $S_{i\mathtt{w}}$ represent, in this order, the saturation and irreducible saturation of the wetting phase, $S_{gr\mathtt{w}}$ is the residual saturation of the non-wetting phase, $kr\mathtt{w}_{max}$ is the maximum water saturation, $kr\mathtt{g}_{max}$ is the maximum gas saturation, $e\mathtt{w}$ and $eo\mathtt{w}$ are the Corey exponents for the water and gas phases, respectively.

The adopted capillary pressure curve originates from models based on power laws [12],

$$p_c(S_{\mathtt{w}}) = p_{c_{max}} \left( \frac{1 - S_{\mathtt{w}} - S_{gr\mathtt{w}}}{1 - S_{i\mathtt{w}} - S_{gr\mathtt{w}}} \right)^{epc}, \tag{13}$$

where the maximum value of the curve, $p_{c_{max}}(S_{i\mathtt{w}})$, and the exponent $epc$ must be determined from experiments or through field data.

The initial condition is defined for an arbitrary time $t_0$. For example, for the variables $p_g = p(x, y, z, t)$ and $S_w = S(x, y, z, t)$, the initial condition is imposed in the form [7]:

$$p(x, y, z, t_0) = p_0(x, y, z) \qquad \text{in the entire } \Omega \tag{14}$$

and

$$S(x, y, z, t_0) = S_0(x, y, z) \qquad \text{in the entire } \Omega, \tag{15}$$

in which $S_0$ represents the saturation throughout the domain $\Omega$ at the initial time.

In petroleum reservoir simulations, it is common to define initial pressures at a given reference depth. Then, the hydrostatic gradient and capillary effects are used to determine the initial values at different reservoir depths [11, 13]. Regarding the boundary conditions, in this work, no-flow conditions are imposed at the reservoir boundaries. Finally, more details on the calculations associated with fluid and rock properties can be found in [13].

## 3 Numerical Solution Methodology

We now proceed to the presentation of the numerical solution methodology employed in this work, which includes the use of the Finite Volume Method, operator splitting, linearizations, a well-reservoir coupling technique, and an iterative method for solving linear systems.

### 3.1 Discretization

In the Finite Volume Method, the non-linear partial differential equations (PDEs) that govern the flow are first integrated in space and time over a finite volume. This procedure ensures that mass and fluxes are conserved in each finite volume and over the entire domain [6]. In this method, the solution domain is divided into finite volumes (cells or blocks) with known, not necessarily equal, dimensions. Within this framework, the average values of pressure and saturation are determined at the centers of the blocks. In the three-dimensional case, each finite volume is represented by a parallelepiped with lengths $\Delta x$, $\Delta y$, and $\Delta z$, in that order, such that

$$\sum_{i=1}^{n_x} \Delta x_i = L_x, \quad \sum_{j=1}^{n_y} \Delta y_j = L_y, \quad \sum_{k=1}^{n_z} \Delta z_k = L_z, \tag{16}$$

where $L_x$, $L_y$, and $L_z$ represent the spatial dimensions of the reservoir, as illustrated in Figure 1. The reservoir is partitioned using a grid composed of $n_x$, $n_y$, and $n_z$ volumes in the directions of the $x$, $y$, and $z$ axes, respectively. The indices $i$, $j$, and $k$ represent the centers of the blocks in the $x$, $y$, and $z$ directions, and their faces are identified by $i \pm 1/2, j, k$, $i, j \pm 1/2, k$, and $i, j, k \pm 1/2$. The commonly used compact notation [13] was adopted, in which the faces of the finite volumes are identified by lowercase letters: $(i - 1/2, j, k) = w$, $(i + 1/2, j, k) = e$,

$(i, j-1/2, k) = n$, $(i, j+1/2, k) = s$, $(i, j, k-1/2) = a$, and $(i, j, k+1/2) = b$ (Figure 2). In the computational grid, the center of block $P$ has coordinates $(i, j, k)$, and for neighboring volumes, we have $(i-1, j, k) = W$, $(i+1, j, k) = E$, $(i, j+1, k) = N$, $(i, j-1, k) = S$, $(i, j, k-1) = B$, and $(i, j, k+1) = A$.

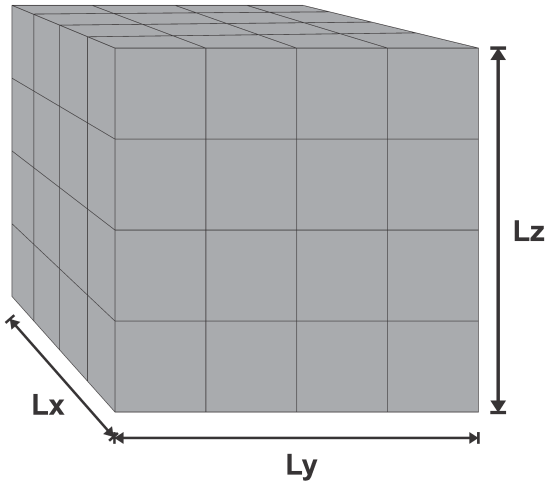


Figure 1: Three-dimensional grid.

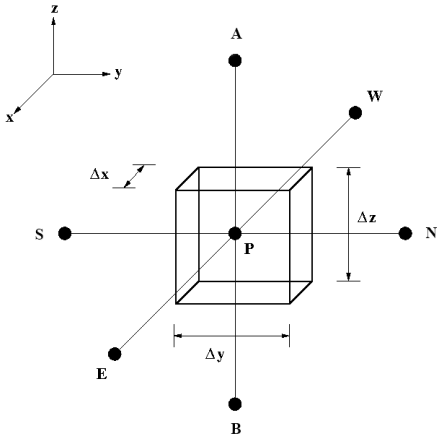


Figure 2: Finite Volume.

The discretization of Equations (9) and (10) begins with an integration over a control volume, as illustrated in Figure 2. Considering the standard development and employing three-point centered difference approximations, their spatially discretized forms are obtained [13]

$$\frac{\partial}{\partial t}\left[\frac{\phi(1-S_{\mathtt{w}})}{B_{\mathtt{g}}}\right]_P V_P = \Delta\left(T_{\mathtt{g}}\Delta p_{\mathtt{g}}\right)_P - \Delta\left(T_{\mathtt{g}}\lambda_{\mathtt{g}}\Delta z\right)_P + q_{scg_P} \tag{17}$$

and

$$\frac{\partial}{\partial t}\left(\frac{\phi S_{\mathtt{w}}}{B_{\mathtt{w}}}\right)_P V_P = \Delta\left(T_{\mathtt{w}}\Delta p_{\mathtt{g}}\right)_P - \Delta\left(T_{\mathtt{w}}\Delta p_c\right)_P - \Delta\left(T_{\mathtt{w}}\lambda_{\mathtt{w}}\Delta z\right)_P + q_{scw_P}, \tag{18}$$

where $V_P = \Delta x_P \Delta y_P \Delta z_P$, $q_{scl_P} = \dot{q}_{scl_P} V_P$, and the operator $\Delta\left(\xi\Delta\eta\right)_P$ was used [11]

$$\Delta\left(\xi\Delta\eta\right)_P \equiv \xi_{x_w}\left(\eta_W - \eta_P\right) + \xi_{x_e}\left(\eta_E - \eta_P\right) + \xi_{y_n}\left(\eta_N - \eta_P\right) + \xi_{y_s}\left(\eta_S - \eta_P\right) + \xi_{z_a}\left(\eta_A - \eta_P\right) + \xi_{z_b}\left(\eta_B - \eta_P\right), \tag{19}$$

and, for two-phase flow, the transmissibilities $T_{lx_f}$ [11] were introduced into Equations (17) and (18):

$$T_{lx_f} \equiv \left(\frac{k_{alx}A_x k_{rl}}{\mu_l B_l \Delta x}\right)_f \qquad l = \mathtt{g}, \mathtt{w}, \tag{20}$$

for $f = w$ or $f = e$. Analogous expressions for transmissibilities can be defined for the $y$ and $z$ directions.

Next, the accumulation terms of Equations (9) and (10) are considered,

$$\frac{\partial}{\partial t}\left[\frac{\phi(1-S_{\mathtt{w}})}{B_g}\right] = \left[\phi\frac{d}{dp_{\mathtt{g}}}\left(\frac{1}{B_{\mathtt{g}}}\right)\right](1-S_{\mathtt{w}})\frac{\partial p_{\mathtt{g}}}{\partial t} + \left[\frac{1}{B_{\mathtt{g}}}\frac{d\phi}{dp_{\mathtt{g}}}\right](1-S_{\mathtt{w}})\frac{\partial p_{\mathtt{g}}}{\partial t} - \left(\frac{\phi}{B_{\mathtt{g}}}\right)\frac{\partial S_{\mathtt{w}}}{\partial t} \tag{21}$$

and

$$\frac{\partial}{\partial t}\left(\frac{\phi S_{\mathtt{w}}}{B_{\mathtt{w}}}\right) = \left[\phi\frac{d}{dp_{\mathtt{w}}}\left(\frac{1}{B_{\mathtt{w}}}\right) + \frac{1}{B_{\mathtt{w}}}\frac{d\phi}{dp_{\mathtt{w}}}\right]S_{\mathtt{w}}\frac{\partial p_{\mathtt{w}}}{\partial t} + \left(\frac{\phi}{B_{\mathtt{w}}}\right)\frac{\partial S_{\mathtt{w}}}{\partial t}. \tag{22}$$

Disregarding the variation of capillary pressure with time [13], $\partial p_c/\partial t = 0$, we have $\partial p_{\mathtt{w}}/\partial t \approx \partial p_{\mathtt{g}}/\partial t$; therefore,

$$\frac{\partial}{\partial t}\left[\frac{\phi(1-S_{\mathtt{w}})}{B_{\mathtt{g}}}\right] = \left[\phi\left(\frac{1}{B_{\mathtt{g}}}\right)' + \frac{\phi'}{B_{\mathtt{g}}}\right](1-S_{\mathtt{w}})\frac{\partial p_{\mathtt{g}}}{\partial t} - \left(\frac{\phi}{B_{\mathtt{g}}}\right)\frac{\partial S_{\mathtt{w}}}{\partial t} \tag{23}$$

and

$$\frac{\partial}{\partial t}\left(\frac{\phi S_{\mathtt{w}}}{B_{\mathtt{w}}}\right) = \left[\phi\left(\frac{1}{B_{\mathtt{w}}}\right)' + \frac{\phi'}{B_{\mathtt{w}}}\right]S_{\mathtt{w}}\frac{\partial p_{\mathtt{g}}}{\partial t} + \left(\frac{\phi}{B_{\mathtt{w}}}\right)\frac{\partial S_{\mathtt{w}}}{\partial t}, \tag{24}$$

where $\phi' = \dfrac{d\phi}{dp_l}$ and $\left(\dfrac{1}{B_l}\right)' = \dfrac{d}{dp_l}\left(\dfrac{1}{B_l}\right)$, $l = \mathtt{g}, \mathtt{w}$ [11].

Substituting Equations (23) and (24) into the right-hand side of Equations (17) and (18) and integrating them in time, we obtain

$$\Delta\left(T_{\mathtt{g}}\Delta p_{\mathtt{g}}\right)_P^{n+1} - \Delta\left(T_{\mathtt{g}}\lambda_{\mathtt{g}}\Delta z\right)_P^{n+1}$$

$$= C_{\mathtt{g}p}\Delta_t p_{\mathtt{g}} + C_{\mathtt{g}s}\Delta_t S_{\mathtt{w}} - q_{sc\mathtt{g}_P}^{n+1} \tag{25}$$

and

$$\Delta\left(T_{\mathtt{w}}\Delta p_{\mathtt{g}}\right)_P^{n+1} - \Delta\left(T_{\mathtt{w}}\Delta p_c\right)_P^{n+1} - \Delta\left(T_{\mathtt{w}}\lambda_{\mathtt{w}}\Delta z\right)_P^{n+1}$$

$$= C_{\mathtt{w}p}\Delta_t p_{\mathtt{g}} + C_{\mathtt{w}s}\Delta_t S_{\mathtt{w}} - q_{sc\mathtt{w}_P}^{n+1} \tag{26}$$

where the coefficients $C$ are given by

$$C_{\mathtt{g}p} = \frac{V_P}{\Delta t}\left\{\left[\phi_P^{n+1}\left(\frac{1}{B_{\mathtt{g}}}\right)_P' + \frac{\phi_P'}{B_{\mathtt{g}P}^n}\right](1 - S_{\mathtt{w}P}^n)\right\}, \tag{27}$$

$$C_{\mathtt{g}s} = -\frac{V_P}{\Delta t}\left(\frac{\phi_P^{n+1}}{B_{\mathtt{g}P}^{n+1}}\right), \tag{28}$$

$$C_{\mathtt{w}p} = \frac{V_P}{\Delta t}\left\{\left[\phi_P^{n+1}\left(\frac{1}{B_{\mathtt{w}}}\right)_P' + \frac{\phi_P'}{B_{\mathtt{w}P}^n}\right] S_{\mathtt{w}P}^n\right\}, \tag{29}$$

and

$$C_{\mathtt{w}s} = \frac{V_P}{\Delta t}\left(\frac{\phi_P^{n+1}}{B_{\mathtt{w}P}^{n+1}}\right), \tag{30}$$

and the operator $\Delta_t\varphi = \varphi_P^{n+1} - \varphi_P^n$ was used.

In Equations (27), (28), (29), and (30), the superscripts $n+1$ and $n$ indicate the future and current time instants, respectively. Additionally, $\Delta t = t^{n+1} - t^n$, with $\phi$, $S_{\mathtt{w}}$, and $B_l$ evaluated at times $n$ or $n+1$ to obtain a conservative approximation in the temporal integration [11]. Equations (25) and (26) therefore result in a fully implicit formulation.

It is assumed that the rocks have a small and constant compressibility. Thus, we have [11]

$$\phi = \phi^0\left[1 + c_\phi(p_{\mathtt{g}} - p^0)\right], \tag{31}$$

where $c_\phi$ is the rock compressibility and $\phi^0$ is the porosity evaluated at the reference pressure $p^0$. The water phase is considered slightly compressible, such that

$$B_{\mathtt{w}} = \frac{B_{\mathtt{w}}^0}{1 + c_w(p_{\mathtt{w}} - p^0)}, \tag{32}$$

where $c_{\mathtt{w}}$ is the water compressibility and $B_{\mathtt{w}}^0$ is the FVF of water at the reference pressure $p^0$. From the definition of the FVF and the real gas law, $B_{\mathtt{g}}$ can be written as [12]

$$B_{\mathtt{g}} = \frac{p_{sc}}{T_{sc}}Z\frac{T}{p_{\mathtt{g}}}, \tag{33}$$

where $p_{sc}$ and $T_{sc}$ are, respectively, the pressure and temperature at standard conditions, and $Z$ is the compressibility factor.

From Equation (31), it is possible to write

$$\phi' = c_\phi\phi^0. \tag{34}$$

Thus, considering Equations (32) and (33),

$$\left(\frac{1}{B_{\mathtt{w}}}\right)' = \frac{c_{\mathtt{w}}}{B_{\mathtt{w}}}, \tag{35}$$

$$\left(\frac{1}{B_{\mathtt{g}}}\right)' = \frac{1}{B_{\mathtt{g}}}\left(\frac{1}{p_{\mathtt{g}}} - \frac{1}{Z}\frac{dZ}{dp_{\mathtt{g}}}\right). \tag{36}$$

Equations (25) and (26) evaluated at the grid volumes form a coupled and non-linear system of algebraic equations. The implementation of the initial and boundary conditions follows the procedures adopted in [13].

Let $it_{n-1}$ be the number of iterations required for the convergence of the solution at the previous time step $\Delta t_{n-1}$. As proposed by [19] and adapted by [13], an empirical criterion is used for the calculation of $\Delta t$, given by

$$\Delta t_n = \begin{cases} n_{decr}\Delta t_{n-1} \text{ if } & it_{n-1} > it_{decr}, \\ n_{incr}\Delta t_{n-1} \text{ if } & it_{n-1} \leq it_{incr}, \\ \Delta t_{n-1} & \text{otherwise}, \end{cases} \tag{37}$$

where $n_{decr}$ and $n_{incr}$ are the decrease and increase rates of the time step, with the iteration number limits established by $it_{decr}$ and $it_{incr}$ ($it_{incr} < it_{decr}$). An upper limit is also imposed on the time step, $\Delta t_n \leq \Delta t_{max}$. If the simulation does not converge, the step is reduced, allowing the continuation of the numerical simulation execution.

### 3.2 Well-Reservoir Coupling

In the adopted well-reservoir coupling model, a horizontal well with radius $r_{wf}$ is considered, and frictional losses and inertial effects within the well are neglected [11]. For each finite volume $c$ traversed by the well, with $c \in \psi_{wf}$, the flow rates of the non-wetting and wetting phases are expressed by [3]:

$$q_{sc\mathtt{g}_c} = -J_{\mathtt{g}_c}\left(p_{\mathtt{g}_c} - p_{wf_c}\right) \tag{38}$$

and

$$q_{sc\mathtt{w}_c} = -J_{\mathtt{w}_c}\left(p_{\mathtt{g}_c} - p_{c_c} - p_{wf_c}\right), \tag{39}$$

where $J_l$ ($l = \mathtt{g}, \mathtt{w}$) represents the productivity index [3] and

$$J_{l_c} = G_{wf_c}\left(\frac{k_{rl_c}}{\mu_{l_c}B_{l_c}}\right). \tag{40}$$

For horizontal wells (parallel to the $x$ direction) [3]

$$G_{wf_c} = \frac{2\pi\sqrt{k_{alz_c}k_{aly_c}}\Delta x_c}{\left[1-\left(\frac{r_{wf}}{r_{eq_c}}\right)^2\right]\ln\left(\frac{r_{eq_c}}{r_{wf}}\right)} \tag{41}$$

where $r_{eq}$ is the equivalent radius given by

$$r_{eq_c} = \sqrt{\frac{\Delta z_c \Delta y_c}{\pi}}\ \exp\left(-0,5\right). \tag{42}$$

Equations (38) and (39) apply to each block $c$ that contains a section of the well ($c \in \psi_{wf}$), and the total flow rate for each phase is the sum of the flow rates of all layers [11],

$$q_{sc\mathtt{g}_{sp}} = -\sum_{c\in\psi_{wf}} J_{\mathtt{g}_c}\left(p_{\mathtt{g}_c} - p_{wf_c}\right) \tag{43}$$

and

$$q_{sc\mathtt{w}_{sp}} = -\sum_{c\in\psi_{wf}} J_{\mathtt{w}_c}\left(p_{\mathtt{g}_c} - p_{c_c} - p_{wf_c}\right). \tag{44}$$

The total production flow rate is obtained by summing the flow rates of all layers, considering both phases [11],

$$q_{sc_{sp}} = -\sum_{c\in\psi_{wf}} J_{\mathtt{g}_c}\left(p_{\mathtt{g}_c} - p_{wf_c}\right) - \sum_{c\in\psi_{wf}} J_{\mathtt{w}_c}\left(p_{\mathtt{g}_c} - p_{c_c} - p_{wf_c}\right), \tag{45}$$

with a production condition in terms of prescribed pressure along the producing well, $p_{wf}$, being adopted in this work.

### 3.3 Linearizations

In this work, linearization techniques are employed, and the transmissibilities at the interfaces $e$, $s$, and $b$ are defined, for example, for the $x$ direction, as

$$T^{n+1}_{lx_e} = \left(\frac{k_{alx}A_x}{\Delta x}\right)_e \left(\frac{1}{\mu_l B_l}\right)^{n+1}_e k^{n+1}_{rl_e}, \tag{46}$$

for $l = \mathtt{g}, \mathtt{w}$, with analogous forms for the $y$ and $z$ directions. Similarly, their expressions at the $w$, $n$, and $a$ faces can be written. They can also be represented as

$$T^{n+1}_{l_f} = G_f F^{n+1}_{p_f} F^{n+1}_{S_f} \tag{47}$$

where the term $G_f$ depends on fluid, rock, and geometric properties, $F^{n+1}_{p_f}$ depends on pressure, and $F^{n+1}_{S_f}$ depends on saturation.

The terms $F^{n+1}_{p_f}$ and $F^{n+1}_{S_f}$ are taken to exemplify how the Picard and Newton-Raphson linearization methods are implemented.

We begin with the Picard iteration, where these terms are evaluated at time $n+1$, but at the previous iterative level $v$. As an example, we have

$$F^{n+1}_{p_e} \approx F^{n+1,v}_{p_e} \tag{48}$$

and

$$F^{n+1}_{S_e} \approx F^{n+1,v}_{S_e}, \tag{49}$$

and the method is conditionally stable [11], with a similar procedure used for the other interfaces.

When the Newton-Raphson method is used, the term at iteration $v+1$ is approximated from its value evaluated at the preceding iteration $v$ [13], yielding, for example,

$$F^{n+1}_{p_e} \approx F^{n+1,v+1}_{p_e} \approx F^{n+1,v}_{p_e} + \left.\frac{\partial F_{p_e}}{\partial p_P}\right|^{n+1,v} \delta p^{n+1,v+1}_{n_P} + \left.\frac{\partial F_{p_e}}{\partial p_E}\right|^{n+1,v} \delta p^{n+1,v+1}_{n_E} \tag{50}$$

and

$$F^{n+1}_{S_e} \approx F^{n+1,v+1}_{S_e} \approx F^{n+1,v}_{S_e} + \left.\frac{\partial F_{p_e}}{\partial S_P}\right|^{n+1,v} \delta S^{n+1,v+1}_{w_P} + \left.\frac{\partial F_{p_e}}{\partial S_E}\right|^{n+1,v} \delta S^{n+1,v+1}_{w_E}, \tag{51}$$

with the properties at the $e$ face determined based on the known values at nodes $P$ and $E$. For the term $F^{n+1}_{S_e}$, the first-order upwind method is used. This method is unconditionally stable [11]. Regarding the accumulation terms, the non-linearities are considered weak (with the exception of gas flow) and are treated using the Picard method. On the other hand, the source terms require a linearization of the type employed for the transmissibilities.

### 3.4 Approximation at Finite Volume Faces

Since transmissibilities must be evaluated at the faces of the finite volumes and pressures and saturations are calculated at the center of the finite volumes, an interpolation must be employed in the calculation of the coefficients at the interfaces. Usually, arithmetic averages (in the case of volumes with the same dimension for the direction under analysis) are used for the pressure terms $F_{p_f}$, ensuring a second-order approximation [11]. For example, we have

$$F_{p_e} = \left(\frac{1}{\mu_l B_l}\right)_e = \frac{1}{2}\left[\left(\frac{1}{\mu_l B_l}\right)_E + \left(\frac{1}{\mu_l B_l}\right)_P\right]. \tag{52}$$

The first-order upwind method is used to prevent possible instabilities associated with centered differences [11] with respect to the saturation-dependent terms, $F_{S_f}$. For example, we use

$$k_{rl_e} = \begin{cases} k_{rl_P} \text{ if } \quad v_e \geq 0, \\ \\ k_{rl_E} \text{ if } \quad v_e < 0, \end{cases} \tag{53}$$

where $v_e$ represents the velocity at the $e$ face.

For the calculation of the term $G_f$, a harmonic average is used for the computation of the apparent permeability, based on what is generally applied for absolute permeability [11]. Considering the area perpendicular to the flow as constant, the geometric term at the $e$ face can be expressed as

$$G_{x_e} = \left(\frac{k_{alx}A_x}{\Delta x}\right)_e = \frac{k_{alx_e}A_{x_e}}{\Delta x_e}, \tag{54}$$

where

$$k_{alx_e} = \frac{k_{alx_P}k_{alx_E}(\Delta x_P + \Delta x_E)}{k_{alx_P}\Delta x_E + k_{alx_E}\Delta x_P}. \tag{55}$$

Analogously, interpolations are performed at the $w$ faces for the $x$ direction, and at the $n$, $s$, $a$, and $b$ faces, taking into account the $y$ and $z$ axes directions.

### 3.5 Hybrid Method

In the present work, the Hybrid Method described in [13] is used. Its objective is to improve numerical stability by implicitly solving, in separate steps, the algebraic systems associated with pressure and saturation. A fully implicit linearization for the wetting phase is employed via the Newton method, using an operator splitting technique [9, 16].

Similar to the Implicit Pressure Explicit Saturation (IMPES) method [11], the pressure equation for each volume can be obtained by combining Equations (25) and (26) such that the term $\Delta_t S_w$ is eliminated. This can be done by multiplying Equation (25) by $B_{\mathtt{g}_P}^{n+1}$, Equation (26) by $B_{\mathtt{w}_P}^{n+1}$, and adding them, noting that $B_{\mathtt{g}_P}^{n+1}C_{\mathtt{gs}} + B_{\mathtt{w}_P}^{n+1}C_{\mathtt{ws}} = 0$. Thus, the pressure equation can be written as [11]

$$\begin{aligned} &B_{\mathtt{g}_P}^{n+1}\Delta\left(T_{\mathtt{g}}\Delta p_{\mathtt{g}}\right)_P^{n+1} + B_{\mathtt{w}_P}^{n+1}\Delta\left(T_{\mathtt{w}}\Delta p_{\mathtt{g}}\right)_P^{n+1} \\ &-B_{\mathtt{w}_P}^{n+1}\Delta\left(T_{\mathtt{w}}\Delta p_c\right)_P^{n+1} - B_{\mathtt{g}_P}^{n+1}\Delta\left(T_{\mathtt{g}}\lambda_{\mathtt{g}}\Delta Z\right)_P^{n+1} \\ &+B_{\mathtt{w}_P}^{n+1}\Delta\left(T_{\mathtt{w}}\lambda_{\mathtt{w}}\Delta Z\right)_P^{n+1} \\ &=(B_{\mathtt{g}_P}^{n+1}C_{\mathtt{g}p} + B_{\mathtt{w}_P}^{n+1}C_{\mathtt{w}p})\Delta_t p_{\mathtt{g}} \\ &-(B_{\mathtt{g}_P}^{n+1}q_{sc\mathtt{g}_P}^{n+1} + B_{\mathtt{w}_P}^{n+1}q_{sc\mathtt{w}_P}^{n+1}), \end{aligned} \tag{56}$$

when calculating the pressures in the porous medium. Once determined at the current time step $(n+1)$ and iteration $(v+1)$, they cease to be unknowns when solving the wetting phase equation, making saturation the only variable to be computed. The fully implicit linearization, in terms of the wetting phase saturation, results in a system of equations that is solved by the Newton-Raphson method. This system can be represented in the following matrix form [13]:

$$\mathbf{J}_{\mathtt{w}}^{n+1,v}\boldsymbol{\delta}\mathbf{S}_{\mathtt{w}}^{n+1,v+1} = -\mathbf{R}_{\mathtt{w}}^{n+1,v}, \tag{57}$$

where $\mathbf{J}_{\mathtt{w}}^{n+1,v}$ represents the Jacobian matrix, $\boldsymbol{\delta}\mathbf{S}_{\mathtt{w}}^{n+1,v+1} = \mathbf{S}_{\mathtt{w}}^{n+1,v+1} - \mathbf{S}_{\mathtt{w}}^{n+1,v}$, and the vector containing the unknowns is

$$\mathbf{S}_{\mathtt{w}} = (S_{\mathtt{w}_1}, S_{\mathtt{w}_2}, S_{\mathtt{w}_3}, ..., S_{\mathtt{w}_N})^T, \tag{58}$$

while for the residual vector $\mathbf{R}_{\mathtt{w}}$ we have

$$\mathbf{R}_{\mathtt{w}} = (R_{\mathtt{w}_1}, R_{\mathtt{w}_2}, R_{\mathtt{w}_3}, ..., R_{\mathtt{w}_N})^T, \tag{59}$$

where $n = 1, 2, 3, ...N$, for a computational grid with $N$ volumes.

After solving the system of linear algebraic equations, the new saturations can be calculated using

$$\mathbf{S}_{\mathtt{w}}^{n+1,v+1} = \mathbf{S}_{\mathtt{w}}^{n+1,v} + \boldsymbol{\delta}\mathbf{S}_{\mathtt{w}}^{n+1,v+1}, \tag{60}$$

applicable to each cell of the computational domain.

For each volume in the grid, using the Newton method, we have [13]

$$\begin{aligned} -R_{\mathtt{w}_P}^{n+1,v} = &\left.\frac{\partial R_{\mathtt{w}_P}}{\partial S_{\mathtt{w}_A}}\right|^{n+1,v} \delta S_{\mathtt{w}_A}^{n+1,v+1} \\ &+ \left.\frac{\partial R_{\mathtt{w}_P}}{\partial S_{\mathtt{w}_N}}\right|^{n+1,v} \delta S_{\mathtt{w}_N}^{n+1,v+1} \\ &+ \left.\frac{\partial R_{\mathtt{w}_P}}{\partial S_{\mathtt{w}_W}}\right|^{n+1,v} \delta S_{\mathtt{w}_W}^{n+1,v+1} \\ &+ \left.\frac{\partial R_{\mathtt{w}_P}}{\partial S_{\mathtt{w}_P}}\right|^{n+1,v} \delta S_{\mathtt{w}_P}^{n+1,v+1} \\ &+ \left.\frac{\partial R_{\mathtt{w}_P}}{\partial S_{\mathtt{w}_E}}\right|^{n+1,v} \delta S_{\mathtt{w}_E}^{n+1,v+1} \\ &+ \left.\frac{\partial R_{\mathtt{w}_P}}{\partial S_{\mathtt{w}_S}}\right|^{n+1,v} \delta S_{\mathtt{w}_S}^{n+1,v+1} \\ &+ \left.\frac{\partial R_{\mathtt{w}_P}}{\partial S_{\mathtt{w}_B}}\right|^{n+1,v} \delta S_{\mathtt{w}_B}^{n+1,v+1} \end{aligned} \tag{61}$$

where

$$R_{\mathtt{w}_P}^{n+1,v} = -T_{\mathtt{w}z_a}^{n+1,v}\Delta\Phi_{\mathtt{w}z_A}^{n+1,v} - T_{\mathtt{w}y_n}^{n+1,v}\Delta\Phi_{\mathtt{w}y_N}^{n+1,v}$$

$$- T_{\mathtt{w}x_w}^{n+1,v}\Delta\Phi_{\mathtt{w}x_W}^{n+1,v} - T_{\mathtt{w}x_e}^{n+1,v}\Delta\Phi_{\mathtt{w}x_E}^{n+1,v}$$

$$- T_{\mathtt{w}y_s}^{n+1,v}\Delta\Phi_{\mathtt{w}y_S}^{n+1,v} - T_{\mathtt{w}z_b}^{n+1,v}\Delta\Phi_{\mathtt{w}z_B}^{n+1,v}$$

$$+ C_{\mathtt{w}p}(p_{\mathtt{g}_P}^{n+1,v} - p_{\mathtt{g}_P}^{n}) + C_{\mathtt{w}s}(S_{\mathtt{w}_P}^{n+1,v} - S_{\mathtt{w}_P}^{n})$$

$$- q_{sc\mathtt{w}_P}^{n+1,v} \tag{62}$$

and, for example,

$$\Delta\Phi_{\mathtt{w}z_A}^{n+1,v} \equiv \left(p_{\mathtt{w}_A}^{n+1,v+1} - p_{\mathtt{w}_P}^{n+1,v+1}\right) - \left(p_{c_A}^{n+1,v} - p_{c_P}^{n+1,v}\right)$$

$$- \lambda_{\mathtt{g}_a}^{n+1,v}\left(z_A - z_P\right), \tag{63}$$

with similar definitions employed for the other terms [13].

The derivatives of the residuals with respect to saturation are obtained consistently with those that can be obtained by the Newton-Raphson method. The implicit calculation of the pressure field in the porous medium is performed in a first step, followed by an equally implicit calculation of the saturation field, using a fully implicit linearization.

This iterative process is conducted until convergence is achieved, following the established criteria. The systems of algebraic equations are solved by applying the Biconjugate Gradient Stabilized method using the ILU-type preconditioner [13].

## 4 Numerical Results

In this work, simulations were carried out considering: Darcy-type flow (Case 1); non-Darcy-type flow with the Klinkenberg effect and correction due to effective stress (Case 2); non-Darcy-type flow with the Klinkenberg effect (Case 3); and non-Darcy-type flow with correction due to effective stress (Case 4).

For the simulations, a basic set of parameters was defined, based on those used by [13] for the study of water-gas flow in a conventional reservoir with production via a vertical well. The parameters necessary for including slippage and effective stress effects were chosen after research in works dedicated to the study of unconventional low-permeability reservoirs, as was done for the horizontal well configuration.

The general parameters for the standard case, including fluid and rock properties and the geometric characteristics of the reservoir, can be found in Table 1. In this table, $g_{cap}$ is the location of the bottom of the gas cap, measured from the top of the reservoir.

For a mesh refinement study, four distinct computational meshes were employed to determine the most suitable one and to verify the numerical convergence of the method [11]. The mesh was refined along all three spatial directions, and the physical characteristics of the porous medium and the operational conditions defined in the reference case were preserved. This study is essential for reducing errors associated with discretization and for ensuring the accuracy of the results. Table 2 contains, for the computational grids employed, the respective numbers of volumes in the $x$, $y$, and $z$ directions, denoted as $n_x$, $n_y$, and $n_z$.

Figures 3 and 4 show the results of this evaluation for Case 2, displaying the gas flow rate and cumulative production curves for each configuration. As the meshes are refined, the flow rate and cumulative production curves become increasingly close to each other, with the exception of the initial region. It should be noted that the adopted well-reservoir coupling technique [20] has an artifact called numerical storage, which appears as plateaus when simulations are performed for a prescribed flow rate and when studying plots of wellbore pressure as function of time, with the time axis on a logarithmic scale. Thus, the results obtained here for the initial periods are under the influence of this artifact, which is reduced by mesh refinement and is dependent on fluid properties, rock properties, and geometry [10].

Table 1 General parameters.

| Parameter | Value | Unit |
|---|---|---|
| $b$ | 1,000 | psi |
| $B_w^0$ | 1.022 | – |
| $c_\phi$ | $4\times10^{-6}$ | psi$^{-1}$ |
| $c_w$ | $1\times10^{-5}$ | psi$^{-1}$ |
| $g_{cap}$ | 90 | ft |
| $k_0$ | $1\times10^{-7}$ | Darcy |
| $k_{rw_{max}}$ | 0.4 | – |
| $k_{rg_{max}}$ | 0.9 | – |
| $L_x = L_y$ | 1,000 | ft |
| $L_z$ | 180 | ft |
| $L_w$ | 500 | ft |
| $p_{sc}$ | 14.696 | psi |
| $p_{wf}$ | 2,000 | psi |
| $p_0 = p^0$ | $4\times10^3$ | psi |
| $r_{wf}$ | 0.1875 | ft |
| $S_{g\mathtt{w}}$ | 0.15 | – |
| $S_{\mathtt{w}0}$ | 0.20 | – |
| $T$ | 609.67 | R |
| $T_{sc}$ | 519.67 | R |
| $\gamma$ | $1\times10^{-4}$ | psi$^{-1}$ |
| $\phi_0$ | 0.07 | – |

Table 2 Meshes.

| Mesh | $n_x$ | $n_y$ | $n_z$ |
|---|---|---|---|
| 1 | 64 | 65 | 22 |
| 2 | 128 | 129 | 42 |
| 3 | 256 | 257 | 82 |
| 4 | 512 | 513 | 162 |

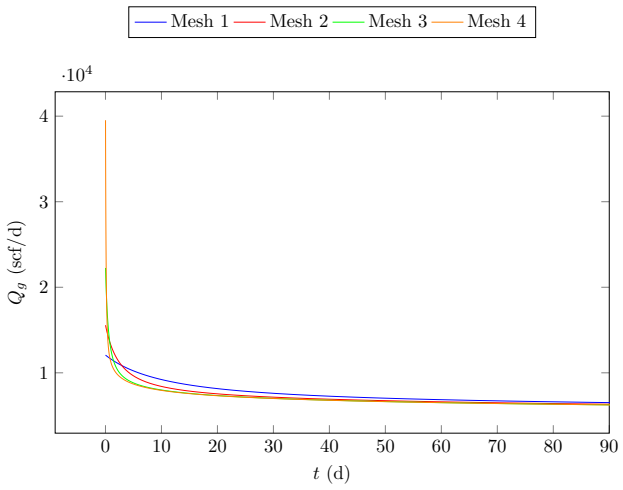


Figure 3: Mesh refinement (Case 2): gas flow rate.

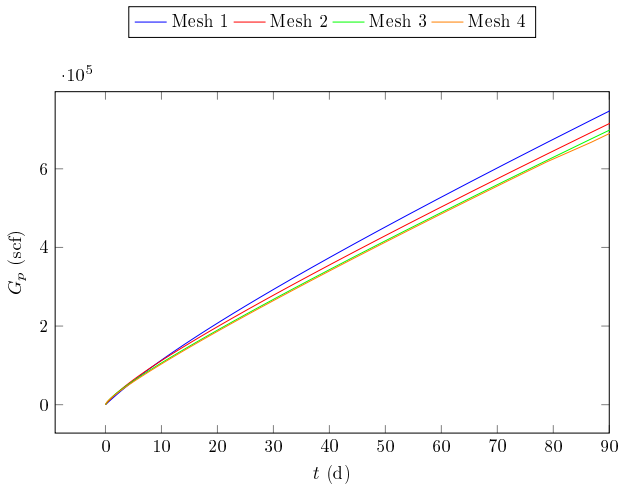


Figure 4: Mesh refinement (Case 2): cumulative gas production.

The comparison of the results revealed that Mesh 3 offers a suitable balance between accuracy and computational cost. This choice was substantiated by the overlap of the curves obtained for the more refined meshes (Mesh 3 and Mesh 4), indicating that the results obtained with Mesh 3 are satisfactory. Furthermore, the utilization of Mesh 3 leads to a reduction in simulation time compared to Mesh 4, rendering it the most effective choice for this study. Consequently, Mesh 3 was employed as the standard mesh in subsequent simulations.

Figures 5 and 6 present a comparison between the flow rate and the cumulative gas production for Cases 1 and 2 over time. In Case 1, only the flow governed by the classical Darcy's Law is considered, whereas Case 2 includes the effects of gas slippage and permeability correction due to effective stress variation.

This comparison allows for the evaluation of how these phenomena influence two-phase flow in low-permeability reservoirs. The results demonstrated that, in Case 2, the gas flow rate is higher compared to Case 1, leading to greater cumulative production over time. This behavior is primarily attributed to the Klinkenberg effect, which elevates the apparent permeability in low-pressure regions, facilitating gas flow through the rock micropores. Conversely, the correction resulting from rock deformation has an opposing effect, decreasing the effective permeability as the reservoir pressure declines. This is caused by the redistribution of mechanical stress, which results in a reduction of the gas transport capacity within the pores, with a consequent drop in reservoir pressure. Nevertheless, the combination of these two effects shows that the positive impact of gas slippage largely compensates for the negative impact of the stress-dependent correction, resulting in an overall superior performance in Case 2 in terms of both gas flow rate and cumulative production.

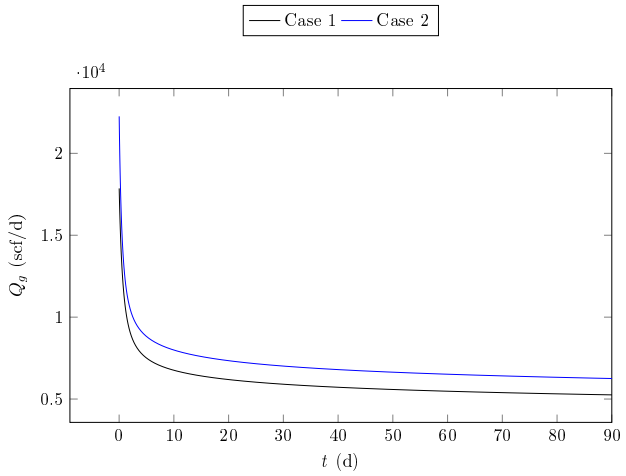


Figure 5: Comparison between Darcy and Non-Darcy cases (including all effects): gas flow rate.

The variation of gas flow rate over time is illustrated in Figure 7, while Figure 8 presents the cumulative gas production, in a comparative analysis of results obtained for Cases 1, 2, 3, and 4. In Case 3, a significant increase in gas flow rate is observed compared to the other cases, exhibiting the highest production. This is attributed to the higher apparent permeability values characteristic of low-permeability gas reservoirs when the Klinkenberg effect is influential. This increase in flow rate directly reflects the enhanced cumulative production. Conversely, Case 4 shows a significant reduction in both flow rate and cumulative production due to the stress-dependent correction effect, which diminishes the transport capacity within the pores resulting from reservoir pressure decline. Thus, the adverse impact of this effect in low-permeability reservoirs is evident.

Referring again to Figures 7 and 8, Case 2, which incorporates all considered effects, exhibits the second highest gas flow rate and cumulative production. Despite the detrimental influence of stress-dependent per-

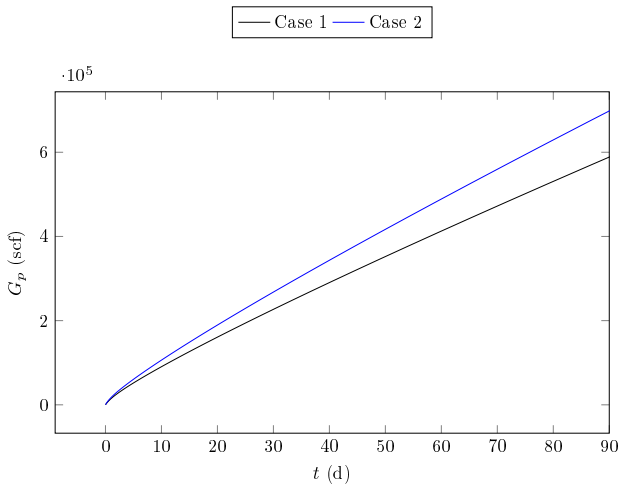


Figure 6: Comparison between Darcy and Non-Darcy cases (including all effects): cumulative gas production.

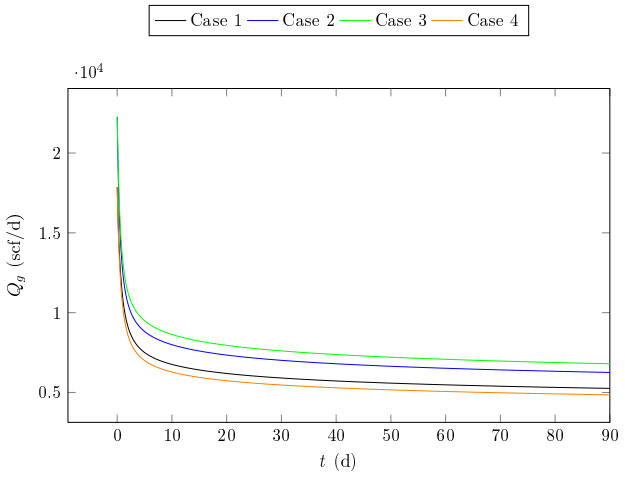


Figure 7: Comparison of all cases: gas flow rate.

meability reduction, the beneficial impact of gas slippage largely counteracts this decrease. Consequently, with respect to both flow rate and cumulative production, Case 2 is surpassed only by Case 3, where this negative stress-dependent impact is absent.

Figures 9 and 10 illustrate the impact of the Klinkenberg effect on gas production across three scenarios: $b$=0 psi (Darcy flow), $b$=500 psi (moderate slippage), and $b$=1,000 psi (base case). The values of this parameter reflect the magnitude of gas slippage's influence within the reservoir, directly affecting the apparent permeability. When $b$=0 psi, mass flow occurs without slippage, resulting in the lowest gas flow rate and cumulative production among the analyzed scenarios.

Further examining Figures 9 and 10, the scenario with $b$=500 psi demonstrates a moderate Klinkenberg effect across the evaluated cases, resulting in an apparent permeability that exceeds that observed in Darcy flow. A noticeable increase in gas flow rate is observed, with the

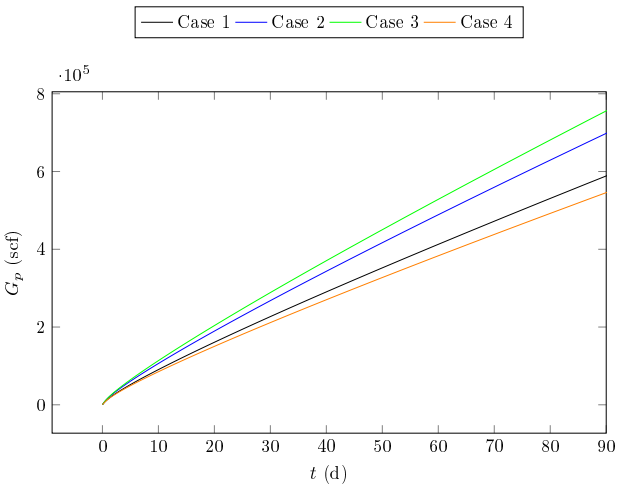


Figure 8: Comparison of all cases: cumulative gas production.

slippage effect being more pronounced in regions of lower pressure (near the wellbore). Consequently, the cumulative production experiences a significant enhancement over time, highlighting the positive impact of slippage on improving production efficiency under low-pressure conditions. Finally, for $b$=1,000 psi (base case), a greater intensity of the slippage effect is present, causing the most substantial increase in apparent permeability. This condition further enhances gas transport and, consequently, leads to the highest gas flow rate and cumulative production over time.

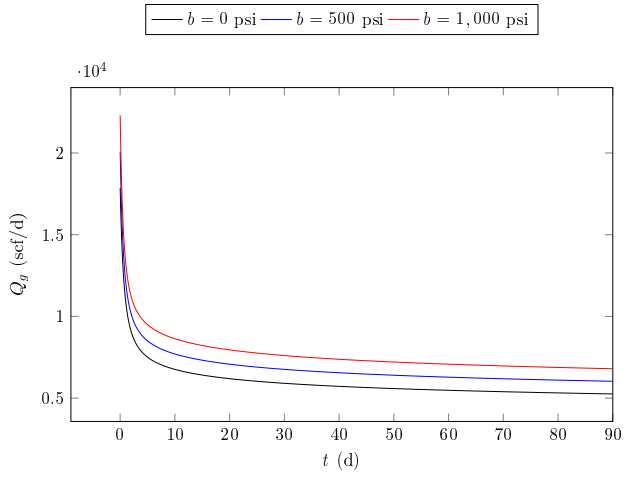


Figure 9: Impact of $b$ variation on the Klinkenberg effect: gas flow rate.

The impact of the coefficient $\gamma$, present in Equation(3), on gas flow rate and cumulative production is illustrated in Figures 11 and 12, respectively. This coefficient influences the stress-induced changes in the matrix permeability values. For $\gamma$=0 psi$^{-1}$, the case of flow governed by the original Darcy's Law is observed. With no compaction of the porous matrix, the absolute perme-

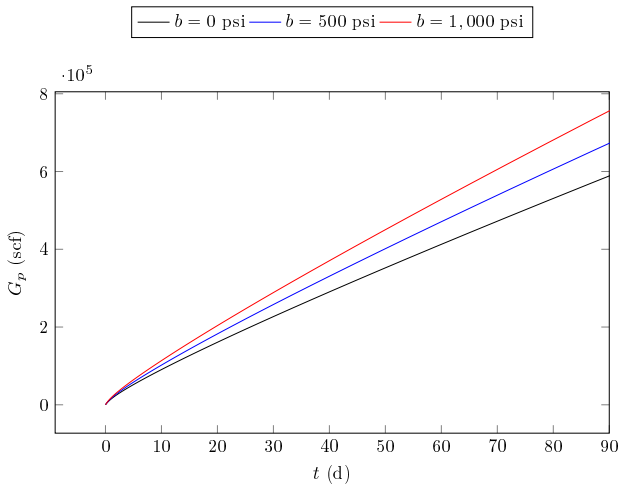


Figure 10: Impact of $b$ variation on the Klinkenberg effect: cumulative gas production.

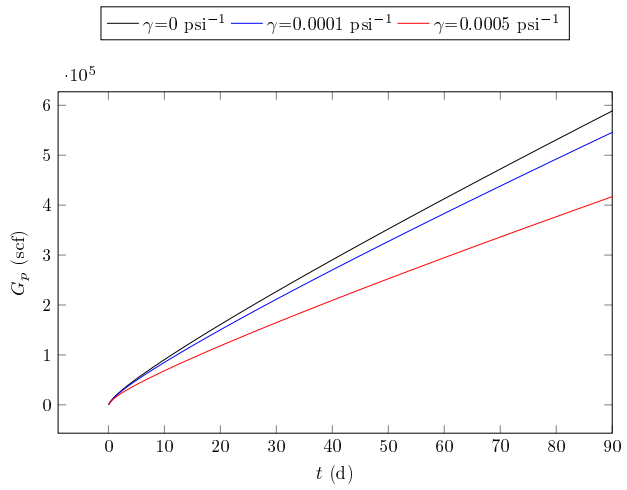


Figure 12: Influence of $\gamma$ on the stress-induced deformation effect: cumulative gas production.

ability remains constant over time, irrespective of the reservoir pressure. A higher gas flow rate and cumulative production are observed, as there is no reduction in the transport capacity through the pores due to rock compaction.

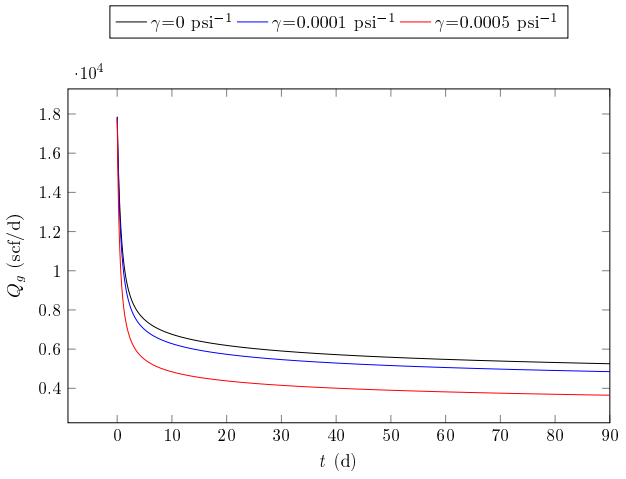


Figure 11: Influence of $\gamma$ on the stress-induced deformation effect: gas flow rate.

As $\gamma$ increases, the negative effects of matrix compaction become more pronounced. For the reference case ($\gamma$=0.0001 psi$^{-1}$), a moderate reduction in absolute permeability occurs, resulting in a comparatively small decrease in gas flow rate and cumulative production. However, for $\gamma$=0.0005 psi$^{-1}$, the effects of compaction intensify, leading to a significant reduction in apparent permeability and consequently a sharp decline in gas flow rate and substantially lower cumulative production.

Moving on, the impact of horizontal well length was investigated, with the results presented in Figures 13 and 14. For $L_w$=400 ft, the limited contact area considerably reduces the capacity of fluids to flow from the rock to the wellbore. Consequently, the gas flow rate is lower, directly reflecting a reduced cumulative production. In the base case, $L_w$=500 ft, an improvement in both gas flow rate and cumulative production is observed. The increased well length allows for a larger contact area with the matrix, enhancing the drainage of gas present in nearby productive zones. Thus, it is evident that the utilization of longer horizontal wells enhances operational effectiveness in low-permeability reservoirs. When $L_w$=600 ft, the well reaches its maximum length for the tested cases. Its greater extent enables even more effective drainage, leading to the highest gas flow rate and cumulative production among the evaluated scenarios.

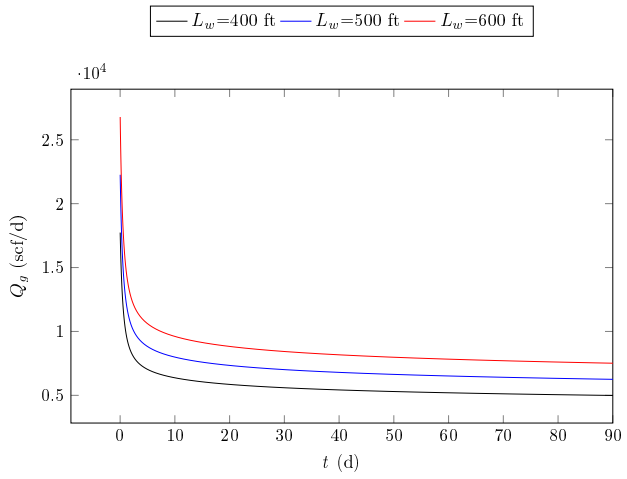


Figure 13: Effect of horizontal well length variation (Case 2): gas flow rate.

The gas flow rate and cumulative production curves for varying porosity values ($\phi$=0.05, 0.07 (reference

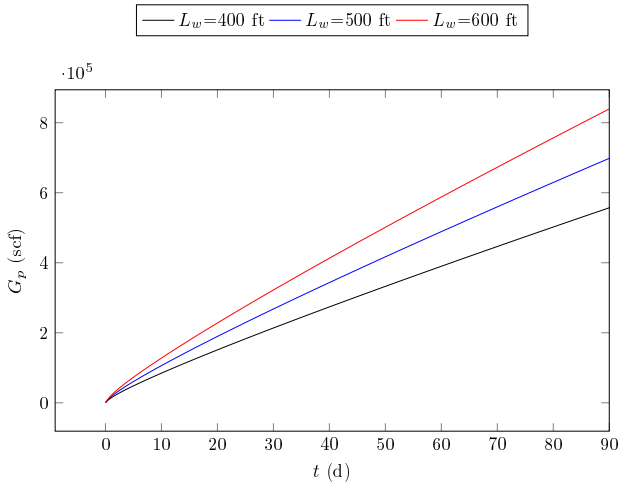


Figure 14: Effect of horizontal well length variation (Case 2): cumulative gas production.

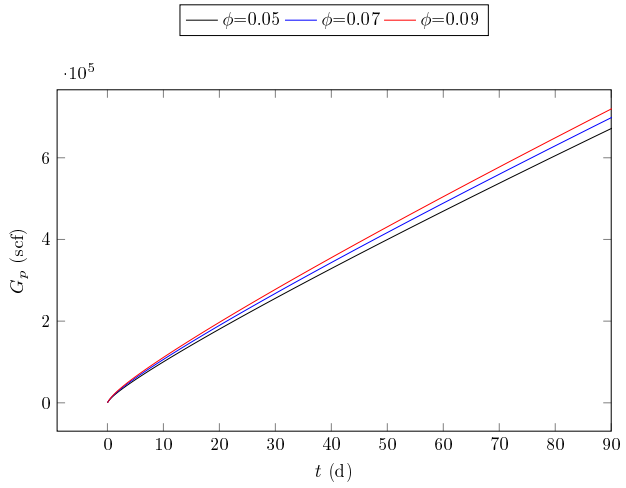


Figure 16: Impact of porosity variation (Case 2): cumulative gas production.

case), and 0.09) are presented in Figures 15 and 16, respectively. It is evident that increasing porosity leads to a higher gas flow rate, as both the storage capacity and transport capability of the gas are directly influenced by this property. A greater porosity value corresponds to a larger volume of gas available for flow.

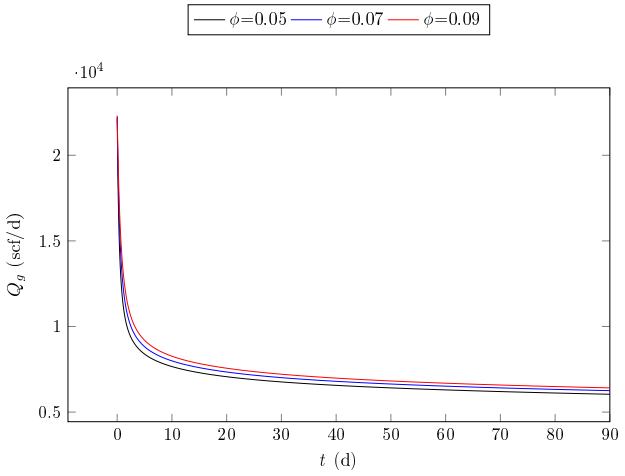


Figure 15: Impact of porosity variation (Case 2): gas flow rate.

For $\phi$=0.05, the flow rate is the lowest due to the reduced storage capacity of the reservoir. In the intermediate case ($\phi$=0.07), an increase in flow rate is observed, demonstrating the positive impact of enhanced porosity. Finally, for $\phi$=0.09, the flow rate is the highest, being more pronounced in the initial stages and gradually declining over time. The cumulative gas production follows the same trend observed for the flow rate. The highest porosity ($\phi$=0.09) results in superior cumulative production, owing to the larger volume of gas stored and available for production. Over time, the difference between the cases becomes more distinct, as the greater storage capacity allows for more sustained production. Conversely, with $\phi$=0.05, the cumulative production is the lowest, limited by the smaller gas volume present in the reservoir. Regarding $\phi$=0.07, an intermediate cumulative production is observed.

Figures 17 and 18 present the analysis of absolute permeability ($k_0$) for gas flow rate and cumulative production, respectively, considering three permeability values.

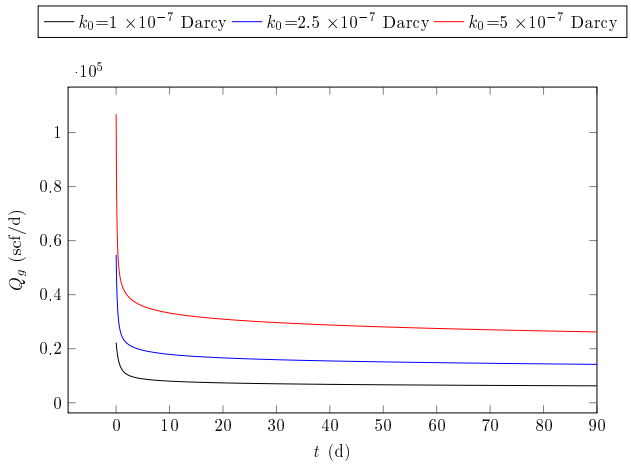


Figure 17: Impact of absolute permeability variation on production (Case 2): gas flow rate.

As the absolute permeability value increases, the initial and final values of both flow rate and cumulative production also increase. For $k_0$=5 $\times 10^{-7}$ Darcy, the initial flow rate is higher, and the decline is slower over time, whereas for $k_0$= 1 $\times 10^{-7}$ Darcy, it is the lowest, indicating greater resistance to gas flow within the reservoir. The cumulative volume produced exhibits similar behavior, as the increase in permeability results in its faster

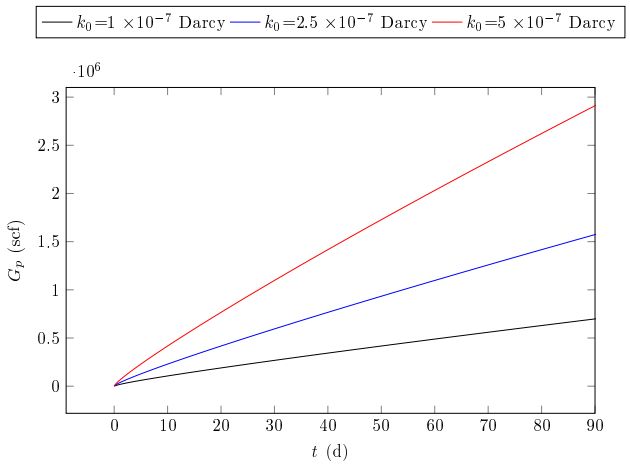


Figure 18: Impact of absolute permeability variation on production (Case 2): cumulative gas production.

growth due to the enhanced ease of fluid flow within the porous medium as a consequence of its increase.

## 5 Conclusion

This work presented numerical simulations aimed at investigating production in low-permeability natural gas reservoirs under two-phase water-gas flow, considering the effects of gas slippage and permeability correction due to effective stress variation. The formulation, based on the Picard-Newton method, successfully captured the typical curves for gas flow rate and cumulative production. It is understood that a quantitative evaluation necessitates a comparison with other results derived from different numerical simulators, experimental data, or analytical solutions for specific cases. Increasing the coefficient $b$ resulted in an enhancement of apparent permeability, demonstrating its relevance in low-permeability reservoirs. Consequently, increases in gas flow rates and cumulative production were observed.

Elevating the modulus $\gamma$ intensified the effects of porous matrix compaction, leading to a decrease in permeability and consequently restricting gas mass flow and negatively impacting cumulative production. As its values were increased, the apparent permeability reduction became more pronounced with declining reservoir pressure. Enhancing porosity exhibited a direct correlation with increased gas flow rate and cumulative production. Higher porosity values lead to a greater gas storage capacity within the reservoir, resulting in improved recovery over time. Regarding the transport capacity through the porous medium, the effect of increasing porosity values is the inverse of that observed with increasing absolute permeability. Concerning absolute permeability, higher values correspond to lower flow resistance. As a consequence, a higher initial flow rate and a slower decline were obtained, yielding a larger cumulative gas volume.

In low-permeability reservoirs, the limitations imposed on flow are significant, thus emphasizing the necessity of employing stimulation techniques to enhance apparent permeability and enable production. In this regard, increasing the length of the horizontal well facilitated a larger contact area with the porous matrix, implying an increase in both gas flow rate and cumulative production. Finally, this study highlights the importance of incorporating accurate models for simulating operational strategies to improve reservoir management.

## References

[1] R. Agrawal and K. Zhang. Flow behavior and challenges in shale gas reservoirs. Journal of Unconventional Oil and Gas Resources, 5:47–61, 2014.

[2] R. F. Aguilera. The Economics of Unconventional Oil and Gas Resources. Springer, Berlin, Germany, 2010.

[3] N.S. Al-Mohannadi. Simulation of Horizontal Well Tests. PhD thesis, Colorado School of Mines, Golden, USA, 2004.

[4] Mohammad Al-Twaijri, Zhaohui Xia, Wei Yu, Liangchao Qu, Yunpeng Hu, Yifei Xu, and Kamy Sepehrnoori. Numerical study of complex fracture geometry effect on two-phase performance of shale-gas wells using the fast EDFM method. Journal of Petroleum Science and Engineering, 164:603–622, 2018.

[5] T. Babadagli, A. Al-Yaseri, and H. Roshan. Physics of fracturing fluid interaction with unconventional reservoirs: Formation damage or enhancement? Journal of Unconventional Oil and Gas Resources, 11:107–121, 2015.

[6] T. Barth, R. Herbin, and M. Ohlberger. Finite Volume Methods: Foundation and Analysis. In E. Stein, R. Borst, and T. J. R. Hughes, editors, Encyclopedia of Computational Mechanics. John Wiley & Sons, Inc, New Jersey, USA, 2 edition, 2017.

[7] Z. Chen, G. Huan, and Y. Ma. Computational Methods for Multiphase Flows in Porous Media. Society of Industrial and Applied Mathematics, Philadelphia, USA, 2006.

[8] C. L. Cipolla, E. Lolon, M. J. Mayerhofer, and N. R. Warpinski. The relationship between fracture complexity, reservoir properties, and fracture-treatment design. SPE Production & Operations, 24(4):575–592, 2009.

[9] J. G. S. Debossam, J. D. S. Heringer, G. Souza, and H. P. A. Souto. Numerical simulation of single-phase flow in naturally fractured oil reservoirs. Coupled Systems Mechanics, 8(2):129–146, 2019.

[10] J. D. dos Santos Heringer, G. de Souza, and H. P. Amaral Souto. On the numerical simulation of non-isothermal heavy oil flow using horizontal wells and horizontal heaters. Brazilian Journal of Chemical Engineering, 41:179–196, 2024.

[11] T. Ertekin, J. H. Abou-Kassem, and G. R. King. Basic Applied Reservoir Simulation. SPE Textbook Series 7. Society of Petroleum Engineers, Richardson, USA, 2001.

[12] N. Ezekwe. Petroleum Reservoir Engineering Practice. Prentice Hall, Westford, USA, 2010.

[13] M. M. Freitas, G. Souza, and H. P. Amaral Souto. A Picard-Newton approach for simulating two-phase flow in petroleum reservoirs. International Journal of Advanced Engineering Research and Science, 7(4):428–457, 2020.

[14] D. Gao and Others. Impact of stress-sensitive permeability on gas production in shale reservoirs. Journal of Natural Gas Science and Engineering, 15:55–67, 2013.

[15] Yong He, Jianjun Wang, Xiaoqing Huang, Yue Du, Xiang Li, Wenshu Zha, and Daolun Li. Investigation of low water recovery based on gas-water two-phase low-velocity non-Darcy flow model for hydraulically fractured horizontal wells in shale. Petroleum, 9(3):364–372, 2023.

[16] J. D. S. Heringer, J. G. S. Debossam, G. Souza, and H. P. A. Souto. Numerical simulation of non-isothermal flow in oil reservoirs using two-equation model. Coupled Systems Mechanics, 8(2):147–168, 2019.

[17] S. A. Holditch. Tight gas sands. Journal of Petroleum Technology, 58(6):86–95, 2006.

[18] L. J. Klinkenberg. The permeability of porous media to liquids and gases. Drilling and Production Practice, American Petroleum Inst., 1:200–213, 1941.

[19] R. D. Mindlin. On the theory of small elastic deformations of bodies with irregular boundaries. Journal of Applied Mechanics, 28:27–32, 1961.

[20] D. W. Peaceman. Interpretation of well-block pressures in numerical reservoir simulation. Society of Petroleum Engineers Journal, 18(3):183–194, 1978.

[21] E. Shahraeeni and A. Firoozabadi. Multiphase flow in tight formations: Challenges and new perspectives. SPE Journal, 20(4):700–711, 2015.

[22] Haibin Wang and Mark D. Zoback. Permeability evolution due to dynamic changes in effective stress during depletion in shale gas reservoirs. Journal of Natural Gas Science and Engineering, 51:102–114, 2018.

[23] Yunfeng Xu, Guanglong Sheng, Hui Zhao, Yanni Hui, Yuhui Zhou, Jialing Ma, Xiang Rao, Xun Zhong, and Jie Gong. A new approach for gas-water flow simulation in multi-fractured horizontal wells of shale gas reservoirs. Journal of Petroleum Science and Engineering, 199:108292, 2021.

[24] Rui-Han Zhang, Lie-Hui Zhang, Hui-Ying Tang, Sheng-Nan Chen, Yu-Long Zhao, Jian-Fa Wu, and Ke-Ren Wang. A simulator for production prediction of multistage fractured horizontal well in shale gas reservoir considering complex fracture geometry. Journal of Natural Gas Science and Engineering, 67:14–29, 2019.

[25] Yunhao Zhang and Daoyong Yang. Modeling two-phase flow behaviour in a shale gas reservoir with complex fracture networks and flow dynamics. Gas Science and Engineering, 119:205112, 2023.